# Density functional study of vibrational and thermodynamic properties of ringwoodite

Yonggang G. Yu[1] and Renata M. Wentzcovitch[1]

[1] Phonon dispersions and vibrational density of states (VDoS) of $Mg_2SiO_4$ ringwoodite have been calculated by first principles as a function of pressure up to 30 GPa using density functional perturbation theory. The predicted zone center frequencies are in close correspondence with existing Raman and infrared experimental data. The pressure dependence of phonon frequencies is linear and agrees well with experiments. The calculated VDoS has then been used in conjunction with the quasi-harmonic approximation to compute the Helmholtz free energy and thermodynamic properties, most of which agree very well with experiments.

**Citation:** Yu, Y. G., and R. M. Wentzcovitch (2006), Density functional study of vibrational and thermodynamic properties of ringwoodite, *J. Geophys. Res.*, *111*, B12202, doi:10.1029/2006JB004282.

## 1. Introduction

[2] $Mg_2SiO_4$ ringwoodite ($\gamma$-spinel phase) is thought to be the most abundant mineral phase in the lower part of Earth's transition zone. Its structural, elastic, and thermodynamic properties affect the dynamics in the transition zone. Although the exact volume fraction of ringwoodite in the transition zone is still unknown, its dissociation into (Mg,Fe)O magnesiowüstite, and $(Mg,Fe)SiO_3$ perovskite, often referred to as postspinel transformation, is believed to be responsible for the 660-km discontinuity that defines the boundary between transition zone and lower mantle [*Dziewonski and Anderson*, 1981]. The exact *P-T* condition of the postspinel transition can serve as a good reference to pressure and temperature at 660 km in Earth. Understanding the above complexities in the transition zone requires a thorough and accurate knowledge on the thermodynamic properties of the iron free end-member, $Mg_2SiO_4$ ringwoodite, over the whole pressure and temperature range of the transition zone. In the past few decades, owing to the development of techniques such as the multianvil apparatus and the laser-heated diamond anvil cell, mantle pressures and temperatures have become accessible in the laboratory. Many high-pressure measurements of thermodynamic properties of ringwoodite [e.g., *Watanabe*, 1982; *Akaogi et al.*, 1989; *Meng et al.*, 1994; *Katsura et al.*, 2004] are available today.

[3] Meanwhile, empirical potential based lattice dynamics [*Price et al.*, 1987] and molecular dynamics [*Matsui*, 1999] calculations, as well as recent first principles based pseudopotential calculations [*Piekarz et al.*, 2002], have been used to predict thermodynamic properties. In particular, Piekarz et al. have obtained a reasonably good agreement with measurements on some thermodynamic properties of ringwoodite using a generalized gradient approximation (GGA) [*Perdew et al.*, 1996] functional. However, considerable improvements on computational results, especially on equation of state parameters, can be made by performing local density approximation (LDA) [*Ceperley and Alder*, 1980]; besides, more detailed and complete calculations of thermodynamic properties of ringwoodite are still needed. Here we have used first principles vibrational density of states (VDoS) in conjunction with the quasi-harmonic approximation (QHA) to obtain the Helmholtz free energy and the thermodynamic properties of $Mg_2SiO_4$ ringwoodite up to 30 GPa.

## 2. Computational Methods

[4] Calculations are performed using one primitive cell with 14 atoms. We have tested both Ceperley-Alder LDA functional as parameterized by *Perdew and Zunger* [1981] and Perdew-Burke-Ernzerhof (PBE) functional for the GGA, but only LDA results are reported here, as they compare more favorably with experimental measurements than GGA, which will be shown later. The pseudopotentials used are the same as those used in previous work [*Karki et al.*, 2000a]. (Pseudopotentials for O and Si were generated by the method of *Troullier and Martins* [1991], while the method of U. von Barth and R. Car (available at http://www.pwscf.org) was used for Mg pseudopotential.)) The plane wave kinetic energy cutoff was chosen to be 70 Ry, and $4 \times 4 \times 4$ (with $(\frac{1}{2} \frac{1}{2} \frac{1}{2})$ shift from origin) Monkhorst-Pack k point mesh [*Monkhorst and Pack*, 1976] was used for Brillouin zone (BZ) samplings. We have checked that the energy converged within $10^{-4}$ Ry/atom with respect to energy cutoff ($E_{pw}$ changing from 70 to 100 Ry) and k point sampling (k point mesh changing from $4 \times 4 \times 4$ to $8 \times 8 \times 8$ and $16 \times 16 \times 16$), while pressure converged to within 0.3 GPa.

[1]Department of Chemical Engineering and Materials Science, Minnesota Supercomputing Institute for Digital Technology and Advanced Computations, University of Minnesota, Minneapolis, Minnesota, USA.

**Table 1.** Calculated Structural Parameters (Wyckoff Positions), Equation of State Parameters, and Thermodynamic Properties at Low Pressures Compared With Experiments for $\gamma$-$Mg_2SiO_4$[a]

| | 300 K, 0 GPa | | 700 K, 4 GPa | |
| --- | --- | --- | --- | --- |
| | Calculated | Experimental | Calculated | Experimental |
| $x$ | 0.0057, 0.0061[b] | 0.0059(1)[c] | 0.0055 | — |
| $V$, Å$^3$ | 527.5 | 526.7(3)[d] | 519.9 | 517.2(0)[d] |
| $K_T$, GPa | 184.6 | 182(3)[d] | 174.9 | 171(4)[d] |
| $\partial K_T/\partial P$ | 4.5 | 4.2(0.3)[d] | 4.6 | 4.4(0.5)[d] |
| $K_S$, GPa | 186 | 185(2),[e] 185(3),[f] 184(3)[g] | | |
| $\alpha$, $\times 10^5$ K$^{-1}$ | 1.97 | 2.54(5),[h] 1.84,[i] 1.8,[d] 1.92,[j] 1.90[b] | | |
| $C_P$, J mol$^{-1}$ K$^{-1}$ | 116.9 | 113.04[k] | | |
| $S$ (J mol$^{-1}$K$^{-1}$) | 85 | 77.43[k] | | |
| $\gamma_{th}$ | 1.24 | 1.25[k] | | |

[a]It has cubic structure (space group Fd$\bar{3}$m). Its primitive cell (2 $Mg_2SiO_4$) has Mg atoms located at 16d with Wyckoff positions $(\frac{1}{2}, 0, 0)$, $(\frac{1}{2}, \frac{1}{4}, \frac{1}{4})$, $(\frac{1}{4}, \frac{1}{4}, \frac{1}{2})$, $(\frac{1}{4}, 0, \frac{3}{4})$, Si atoms located at 8a with Wyckoff positions $(\frac{5}{8}, \frac{1}{8}, \frac{5}{8})$, $(\frac{3}{8}, \frac{3}{8}, \frac{7}{8})$, O atoms located at 32e with Wyckoff positions $(\frac{1}{2}+x, \frac{1}{4}-x, \frac{1}{2}+x)$, $(\frac{1}{2}+x, x, \frac{3}{4}-x)$, $(\frac{3}{4}-x, x, \frac{1}{2}+x)$, $(\frac{3}{4}-x, \frac{1}{4}-x, \frac{3}{4}-x)$, $(\frac{1}{2}+x, \frac{1}{2}+x, \frac{3}{4}+x)$, $(\frac{1}{2}-x, \frac{1}{2}-x, \frac{3}{4}+x)$, $(\frac{1}{4}+x, \frac{1}{2}-x, 1-x)$, $(\frac{1}{2}-x, \frac{1}{4}+x, 1-x)$.

[b]*Piekarz et al.* [2002].
[c]*Hazen et al.* [1993].
[d]*Meng et al.* [1994].
[e]*Li* [2003].
[f]*Jackson et al.* [2000].
[g]*Weidner et al.* [1984].
[h]*Katsura et al.* [2004].
[i]*Chopelas* [2000].
[j]*Suzuki et al.* [1979].
[k]*Chopelas et al.* [1994], reason for the entropy difference is explained in section 4.

[5] Phonon frequencies were obtained by diagonalizing the dynamical matrix whose elements were obtained using density functional perturbation theory (DFPT) [*Baroni et al.*, 2001]. Internal atomic coordinates (for oxygen) were optimized under cubic symmetry before computing vibrational density of states. For each volume, the dynamical matrices were computed on a $2 \times 2 \times 2$ q point grid and then interpolated to a $16 \times 16 \times 16$ grid to produce the normal mode frequencies. This is equivalent to sampling atomic motions in a supercell containing 57344 atoms. The same method has been successfully applied to MgO, $MgSiO_3$ perovskite, $SiO_2$ polymorphs, ilmenite, and $MgSiO_3$ postperovskite [*Karki et al.*, 2000a, 2000b; *Tsuchiya et al.*, 2004; *Wentzcovitch et al.*, 2004b; *Tsuchiya et al.*, 2005]. Computational details can be found in them.

## 3. Vibrational Properties

[6] $Mg_2SiO_4$ ringwoodite is cubic and exists in a $\gamma$-spinel structure that belongs to space group Fd$\bar{3}$m ($O_h^7$) ([*Hazen et al.*, 1993]). This cubic structure consists of isolated $SiO_4$ tetrahedra, with Mg atoms occupying the interstitial sites between $SiO_4$ groups. Experimental and calculated Wyckoff positions are shown in Table 1. The primitive cell has 2 formula units including 14 atoms (Figure 1), so there are 42 normal modes for each point in the Brillouin zone, among which 3 are acoustic and 39 are optical modes as shown in Figure 2. The optical modes at the BZ center may be divided by symmetry as

$$\Gamma_{op} = A_{1g}(R) + E_g(R) + T_{1g} + 3T_{2g}(R) + 2A_{2u} + 2E_u \\ + 4T_{1u}(IR) + 2T_{2u}. \tag{1}$$

Here subscripts g and u denote symmetric and antisymmetric modes with respect to the center of inversion, while R and IR represent Raman and infrared active modes.

[7] Experiments show 5 distinct Raman [*Chopelas et al.*, 1994] and 4 distinct infrared [*Akaogi et al.*, 1984] vibrational frequencies in ringwoodite (The other modes are silent). Symmetry analysis of the normal modes reveals the respective atomic displacements (Figure 1). However, symmetry assignments are difficult in experiments. At ambient pressure, our Raman frequencies range from 309 to 831 cm$^{-1}$. The highest frequency Raman mode (831 cm$^{-1}$) with $A_{1g}$ symmetry, corresponds to pure Si-O bond stretching, i.e., pure $SiO_4$ tetrahedral breathing-type deformation. The $E_g$ modes (375 cm$^{-1}$) consist of pure Si-O bond bending, i.e., $SiO_4$ tetrahedral shape deformation. The $T_{2g}$ modes (309, 586, and 817 cm$^{-1}$) can be viewed as opposite oscillations of the two tetrahedral centers to which internal deformations are superposed. Mg atoms remain still in all Raman modes. The $A_{1g}$ (831 cm$^{-1}$), $E_g$ (375 cm$^{-1}$), and one $T_{2g}$ (817 cm$^{-1}$) mode are shown in Figure 1. The other $T_{2g}$ modes (309 and 586 cm$^{-1}$) also have silicons oscillating in opposite directions but vibrations associated with these modes are more complex and we will not draw them here. In $A_{1g}$ and $E_g$ modes, silicon atoms stand still, while in all triply degenerate $T_{2g}$ modes, they oscillate in opposite directions. In ringwoodite all infrared modes have $T_{1u}$ symmetry. At ambient pressure, the calculated $T_{1u}$ mode frequencies are in very good agreement with experiments [*Akaogi et al.*, 1984] (see Table 2).

[8] Figure 3 shows the pressure dependence of zone center Raman frequencies. Solid lines with triangles denote our computed phonon frequencies. They are much closer to the experimental values (solid squares [*Chopelas et al.*, 1994]) than previous DFT calculations (dashed lines [*Piekarz et al.*, 2002]). All frequencies increase with
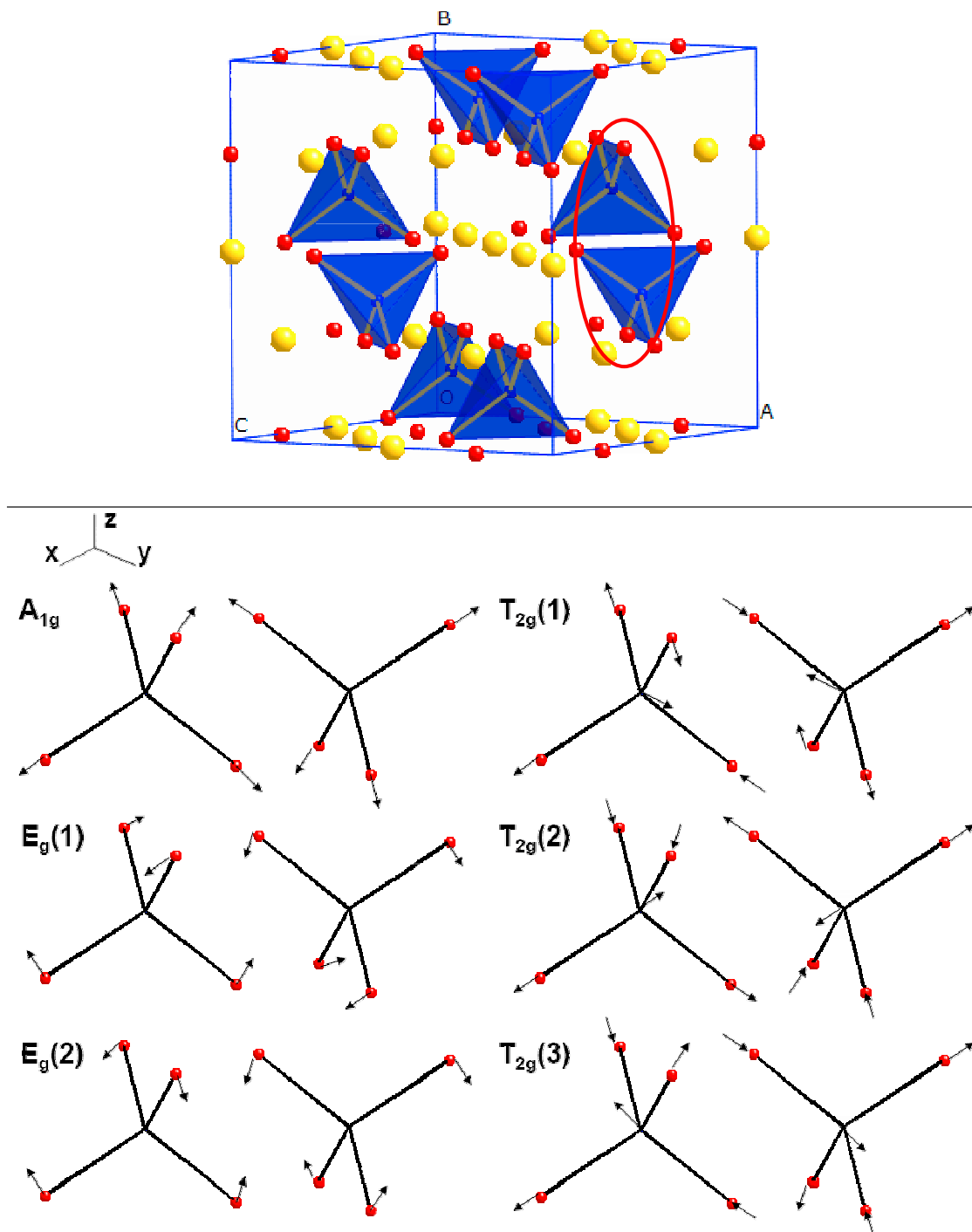
**Figure 1.** Atomic displacements for the pair of $SiO_4$ tetrahedra (in primitive cell) for Raman active modes at 0 GPa in $Mg_2SiO_4$ ringwoodite. Red spheres denote oxygen atoms. At the center of the tetrahedra are Si atoms. The frequency of $A_{1g}$ is 831 cm$^{-1}$, $E_g(1)$ and $E_g(2)$ 375 cm$^{-1}$, and $T_{2g}(1)$, $T_{2g}(2)$, and $T_{2g}(3)$ 817 cm$^{-1}$.

pressure. Our predictions coincide well with experiments for $A_{1g}$, $E_g$, and the lowest $T_{2g}$ modes, but deviate by ∼3% from measurements for the other two $T_{2g}$ modes. Deviations from experimental data in Figure 3 may be due to measurement uncertainties or anharmonic effects not included in our computations.

[9] At 0 GPa, experimentally measured Raman and infrared frequencies at Γ point are highlighted by dots (4 red dots for infrared modes and 5 blue dots for Raman modes) in Figure 2a. The only phonon band gap at Γ point is about 230 cm$^{-1}$ at 0 GPa (Figure 2a) and 280 cm$^{-1}$ at 20 GPa (Figure 2b), showing a tendency to increase with
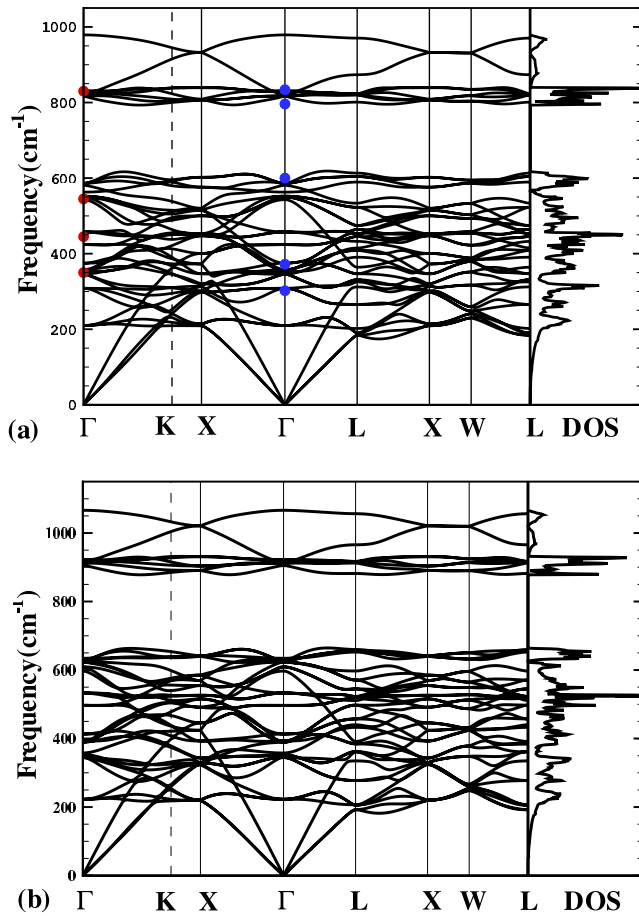
**Figure 2.** Phonon dispersion and vibrational density of states for $Mg_2SiO_4$ ringwoodite (a) 0 GPa and (b) 20 GPa. Four red dots are from infrared experiments [*Chopelas et al.*, 1994], and five blue dots represent Raman data [*Akaogi et al.*, 1984]. These experimental data are also shown in Table 2.

pressure. It appears that this happens because pressure affects the stiffer Si-O bond stretching modes more than it does the softer vibrations (e.g., Si-O bond bending modes). The result is a wider splitting between the upper and lower phonon bands at high pressure than at low pressure. This trend is observed in Figure 3, since clearly the $A_{1g}$ and the highest $T_{2g}$ modes have larger pressure gradient than the other Raman modes.

[10] The LO-TO splitting is quite small to be observed in ringwoodite. We did not observe any signs of phonon softening up to 30 GPa; therefore the dissociation of $Mg_2SiO_4$ ringwoodite into an aggregate of $MgSiO_3$ perovskite and MgO periclase should not result from a mechan-

**Table 2.** Vibrational Modes of $\gamma$-$Mg_2SiO_4$ at Ambient Conditions[a]

| $T_{2g}$ (R) | $E_g$ (R) | $T_{2g}$ (R) | $T_{2g}$ (R) | $A_g$ (R) | $T_{1u}$ (IR) | $T_{1u}$ (IR) | $T_{1u}$ (IR) | $T_{1u}$ (IR) | Reference |
|---|---|---|---|---|---|---|---|---|---|
| 309 | 375 | 586 | 817 | 831 | 345 | 423 | 549 | 829 | this work |
| 302 | 372 | 600 | 796 | 834 | | | | | [b] |
| 302[c] | 370[c] | 600[c] | 794[c] | 836[c] | 350[d] | 445[d] | 545[d] | 830[d] | [c,d] |

[a]In $cm^{-1}$.
[b]*Chopelas et al.* [1994].
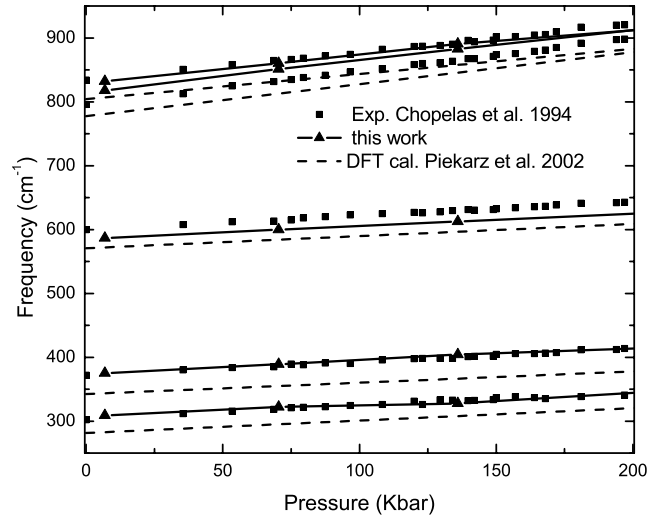[c]*McMillan and Akaogi* [1987].
[d]*Akaogi et al.* [1984].



**Figure 3.** Pressure dependence of the Raman frequencies.

ical instability of the $\gamma$-spinel structure but rather from a general competition in free energy between different phases.

## 4. Thermodynamic Properties

[11] Within the QHA, the Helmholtz free energy is expressed as

$$F(V, T) = U_0(V) + \frac{1}{2} \sum_{\mathbf{q},j} \hbar \omega_j(\mathbf{q}, V) + k_B T \sum_{\mathbf{q},j} \ln$$
$$\cdot \left[1 - \exp\left(-\hbar \omega_j(\mathbf{q}, V)/k_B T\right)\right], \tag{2}$$

where the first term stands for the static internal energy, the second one for zero point motion, and the third one for harmonic vibrational contributions. Summation is taken on a $16 \times 16 \times 16$ mesh in q space; using symmetry, only 74 distinct points are needed in the first BZ. Phonon frequencies are calculated following structural relaxations for each volume (or pressure). The QHA is expected to work well within its validity limit. Superlinear and sublinear deviations in the thermal expansivity at high temperature serves as markers of this limit ([*Wentzcovitch et al.*, 2004a]).

[12] The fundamental thermodynamic quantities are then derived after fitting a fourth-order finite strain equation of state (EoS) to the calculated free energy versus volume at each temperature. Some calculated isothermal compressional curves are compared with experimental data and shown in Figure 4. At 300 K, the LDA volumes match remarkably the experiment while the previous GGA calculations overestimate the volumes by roughly 2.5%. Including the temperature contribution to the free energy at 300 K will increase the equilibrium volume by ~1% and decrease the bulk modulus by ~9.2 GPa relative to the static values. At high temperatures, LDA still overestimates the volumes but only by around 0.5% compared with experiments. Table 1 summarizes the calculated EoS parameters at ambient conditions and at 700 K and 4 GPa. Our results fall within experimental uncertainties.

[13] The coefficient of thermal expansion, $\alpha = 1/V(\partial V/\partial T)_P$, is determined from the equilibrium volume variation with respect to temperature at each pressure (Figure 5). At 0 GPa, the predicted curve lies above values obtained from experimental measurement by *Akaogi et al.* [1989], and
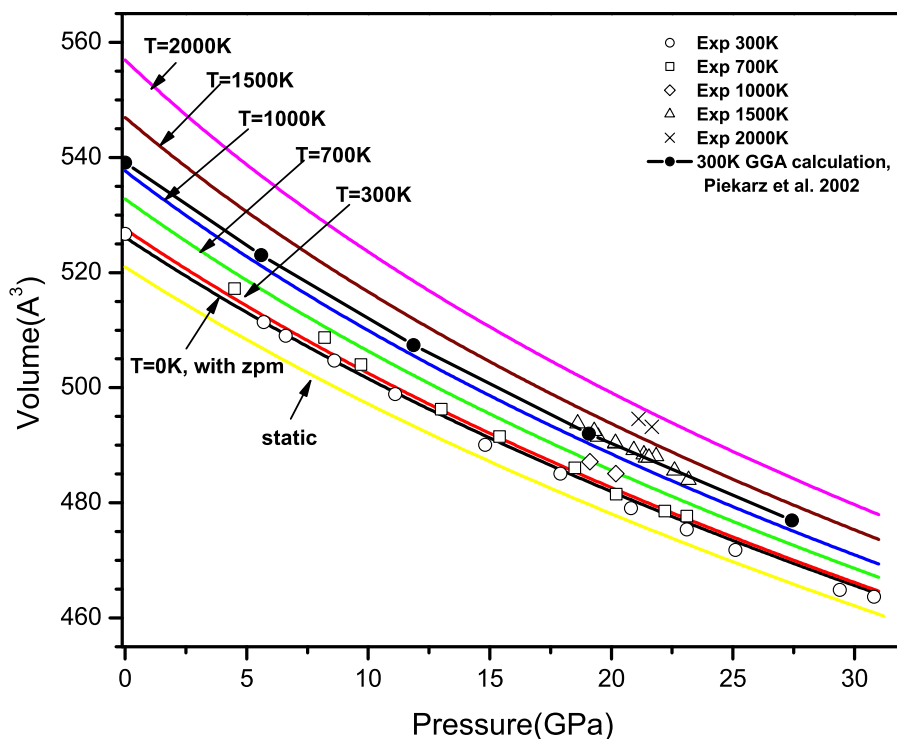
**Figure 4.** Compression curves for static lattice (without zero point motion) and along 0, 300, 700, 1000, 1500, and 2000 K isotherms. Experimental data at each corresponding temperature are denoted by circles, squares, diamonds, triangles, and crosses, respectively [*Katsura et al.*, 2004].

below the values obtained by *Katsura et al.* [2004]. The previous GGA result is closer to this work at low temperature than above 700 K, which also results from the overestimate in volume by GGA. At 21 GPa, up to 1500 K, our calculation agrees with values derived from high *P-T* experiments by *Katsura et al.* [2004]. Above 1500 K, they deviate. Our results appear to fall within the range of experimental values. From this plot we see clearly the validity limit of the QHA, beyond which the lines are dashed.

[14] The dimensionless thermodynamic Grüneisen parameter can be expressed as $\gamma_{th} \equiv \alpha K_S V / C_P = \alpha K_T V / C_V$, or in another form $C_P / C_V = K_S / K_V = 1 + \gamma_{th} \alpha T$, where $\alpha$, $K_T$, $K_S$, $K_S$, $C_V$, and $C_P$ stand for the thermal expansion coefficient, isothermal bulk modulus, adiabatic bulk modulus, heat capacity at constant volume and at constant pressure respectively. The Grüneisen parameter calculated from LDA at ambient pressure (Figure 6), 1.24, agrees well with the experimental value, 1.25 [*Chopelas et al.*, 1994]. Our results show that at 0 GPa, $\gamma_{th}$ varies from 1.25 to 1.4 between 300 K and 2500 K, and at constant temperature it decreases with increasing pressure. At high pressures ($P \sim$ 30 GPa), $\gamma_{th}$ tends to a constant (1.0−1.1 between 1000 K and 3000 K) with a very small linear $T$ dependence.

[15] $C_P$ can be obtained from the relation $C_P = C_V(1 + \gamma_{th} \alpha T)$. As shown in Figure 7a, at ambient conditions, $C_P$ from LDA calculations is closer to *Chopelas et al.*'s [1994] data, but it is different from other groups' data [*Akaogi et al.*, 1989]. At 21 GPa, our calculated $C_P$ values compare favorably with *Katsura et al.*'s [2004] data, except at temperatures above 1800K, which could be due to high-temperature anharmonic effects neglected in the QHA

method. Figure 7b shows $C_V$ along various isobars. Similar to Figure 7a for $C_P$, at 21 GPa our predicted $C_V$ is larger than the experimental results by *Katsura et al.* [2004] but within good tolerance.

[16] From Figure 8a we see that the temperature gradient of the entropy along isobars is positive, while in Figure 8b we see that the pressure gradient of the entropy along isotherms is negative. The former positive gradient results from the basic relation $(\partial S / \partial T)_P = C_P / T$, obviously positive. The latter negative gradient is a consequence of Maxwell's
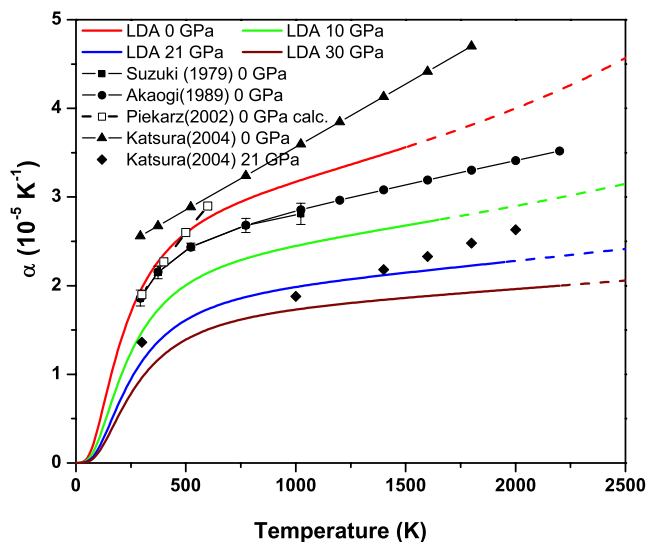


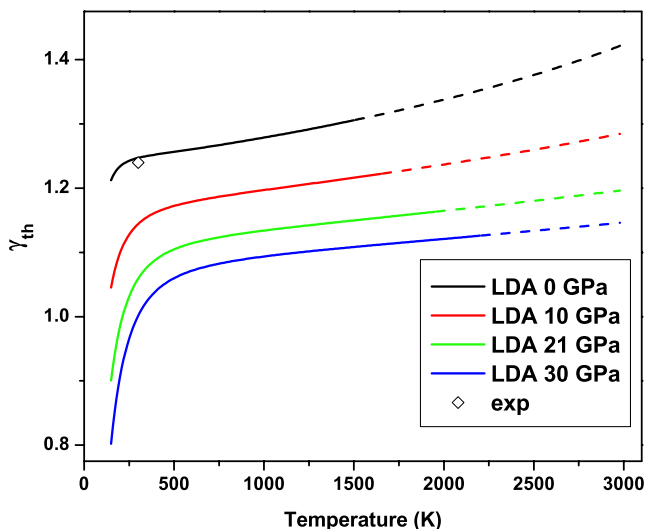**Figure 5.** Thermal expansion coefficient along 0, 10, 21, and 30 GPa isobars.

**Figure 6.** Temperature dependence of the thermal Grüneisen parameter along the isobars at 0, 10, 21, and 30 GPa. Previous result derived from experiment is denoted by diamond [*Chopelas et al.*, 1994].

relation: $(\partial S/\partial P)_T = -(\partial V/\partial T)_P = -V\alpha$, which is negative in this case. In Figure 8b the difference between our calculations and experimental estimates by *Chopelas et al.* [1994] comes mainly from the limited number of phonon frequencies used when deriving thermodynamic properties: only 5 Raman, 4 infrared phonon frequencies, and other previous experimental elasticity and volume data were used. Although the absolute values of calculated and experimentally estimated entropy differ, the change of entropy with temperature agrees quite well.

[17] Figure 9a shows the calculated temperature dependence of adiabatic bulk modulus ($K_S$) at 0, 10, and 21 GPa. At ambient pressure it compares much better with experiments than the previous GGA calculations, which underestimate $K_S$ by about 10 GPa. At 900 K, we obtain $(\partial K_S/\partial T)_P = -0.019$ GPa/K, which is in agreement with experimental values of $-0.020$ GPa/K by *Meng et al.* [1993, 1994] and $-0.024(3)$ GPa/K by *Jackson et al.* [2000]. Figure 9b shows that the slight underestimate of density with respect to the experiment [*Jackson et al.*, 2000] is $\sim$2.3%. Note that comparing with volume data from *Meng et al.* [1994], we only overestimate the volume by $\sim$0.5% at 700 K, 4 GPa.
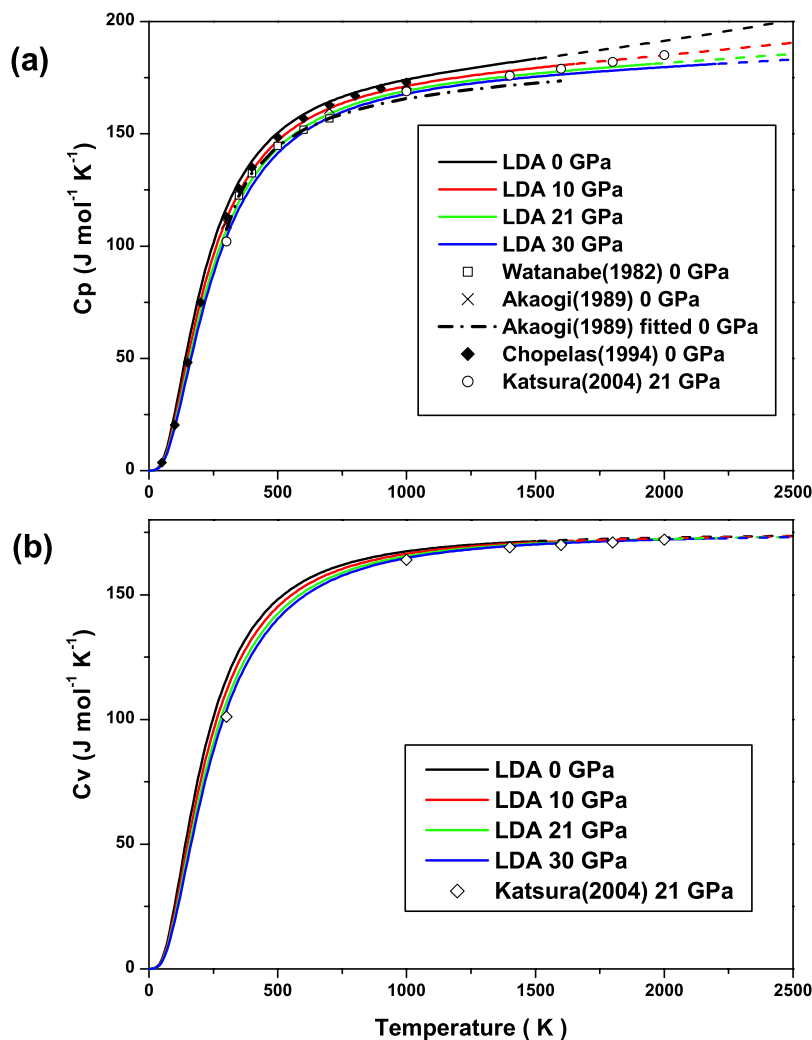


**Figure 7.** Temperature dependence of specific heat (a) Cp and (b) Cv along the isobars at 0, 10, 21, and 30 GPa. Experimental measurements and fitted results at ambient conditions and high pressures are denoted by symbols and dashed lines [*Akaogi et al.*, 1984, 1989; *Chopelas et al.*, 1994; *Katsura et al.*, 2004].
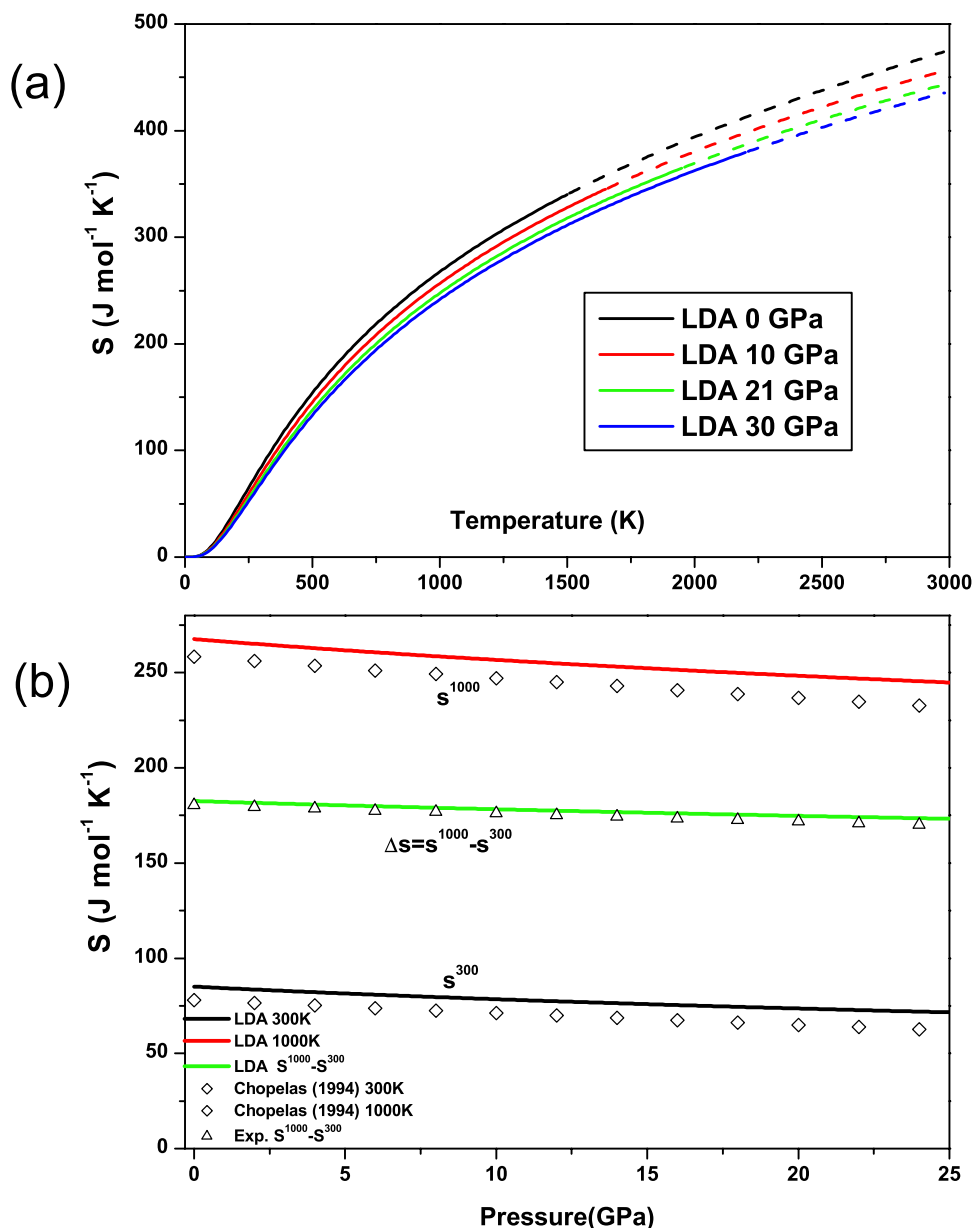
**Figure 8.** (a) Temperature and (b) pressure dependence of entropy. Symbols represent experimental data [*Chopelas et al.*, 1994].

The calculated bulk sound velocity $V_\Phi$ ($\sqrt{K_S/\rho}$) falls within experimental uncertainties. The differences between theory and experiment might originate in anharmonic effects not included in our calculation, even though the temperatures addressed in Figure 9 fall within the range of validity of the QHA. The contribution to these discrepancies from uncertainties in high-temperature and high-pressure measurements cannot be ignored.

[18] Finally, thermodynamic properties of ringwoodite obtained from our calculations are in excellent agreement with experimental data. The GGA calculations of *Piekarz et al.* [2002] exhibit considerably larger deviations from experiments. Comparison between our results and their GGA results have been shown extensively in Table 1 and Figure 3, 4, 5, and 9. Once again, we see that LDA offers

much better structure and thermodynamic properties than GGA for Earth minerals.

## 5. Concluding Remarks

[19] Using DFPT, we have calculated, up to 30 GPa, phonon dispersions and VDoS for ringwoodite ($\gamma$-$Mg_2SiO_4$), a major mineral phase in the transition zone. The pressure dependence of 5 Raman frequencies is linear and agrees well with experimental measurements. Several physical quantities of interest are derived from quasi-harmonic free energy computations and show excellent agreement with various sets of experimental data. We see that the LDA offers results in much better agreement with experiments, mostly within experimental uncertainties, than the GGA. As the temperature uncertainties, uncertainties in pressure
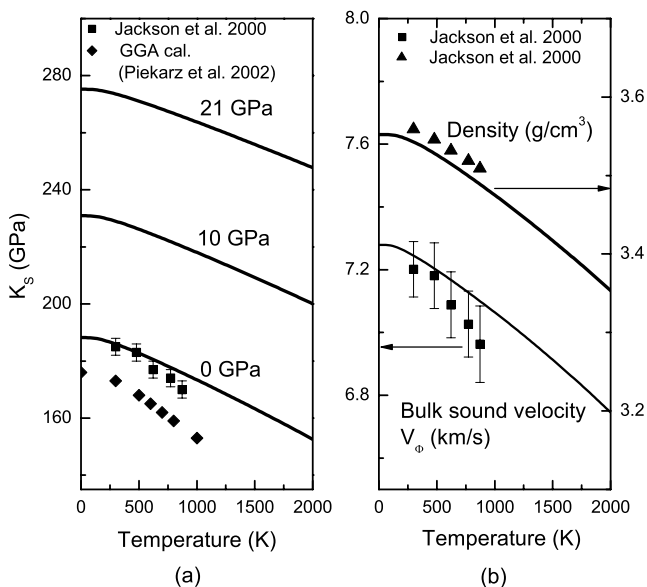
**Figure 9.** Temperature dependence of (a) adiabatic bulk modulus under various pressure compared with experiments ([*Jackson et al.*, 2000]) and previous calculation ([*Piekarz et al.*, 2002]) and (b) bulk sound velocity and density at ambient pressure.

scale, and unknown pressure effects on the thermal couple, etc., weakens the consensus among experiments, our calculation is a helpful reference to understanding properties of this important mineral.

## References

Akaogi, M., N. L. Ross, P. McMillan, and A. Navrotsky (1984), The Mg₂SiO₄ polymorphs (olivine, modified spinel and spinel) – thermodynamic properties from oxide melt solution calorimetry, phase relations, and models of lattice vibrations, *Am. Mineral.*, 69, 499–512.

Akaogi, M., E. Ito, and A. Navrotsky (1989), Olivine-modified spinel-spinel transitions in the system Mg₂SiO₄–Fe₂SiO₄: Calorimetric measurements, thermochemical calculation, and geophysical application, *J. Geophys. Res.*, 94, 15,671–15,685.

Baroni, S., S. de Gironcoli, A. D. Corso, and P. Giannozzi (2001), Phonons and related crystal properties from density-functional perturbation theory, *Rev. Mod. Phys.*, 73, 515–562.

Ceperley, D. M., and B. J. Alder (1980), Ground state of the electron gas by a stochastic method, *Phys. Rev. Lett.*, 45, 566–569.

Chopelas, A. (2000), Thermal expansivity of mantle relevant magnesium silicates from vibrational spectroscopy at high pressures, *Am. Mineral.*, 85, 270–278.

Chopelas, A., R. Boehler, and T. Ko (1994), Thermodynamics and behavior of γ-Mg₂SiO₄ at high-pressure: Implications for Mg₂SiO₄ phase equilibrium, *Phys. Chem. Mineral.*, 21, 351–359.

Dziewonski, A. M., and D. L. Anderson (1981), Preliminary reference Earth model, *Phys. Earth Planet. Inter.*, 25, 297–356, doi:10.1016/0031-9201(81)90046-7.

Hazen, R. M., R. T. Downs, L. W. Finger, and J. Ko (1993), Crystal chemistry of ferromagnesian silicate spinels: Evidence for Mg-Si disorder, *Am. Mineral.*, 78, 1320–1323.

Jackson, J., S. V. Sinogeikin, and J. Bass (2000), Sound velocities and elastic properties of γ-Mg₂SiO₄ to 873 K by Brillouin spectroscopy, *Am. Mineral.*, 85, 296–303.

Karki, B. B., R. M. Wentzcovitch, S. de Gironcoli, and S. Baroni (2000a), Ab initio lattice dynamics of MgSiO₃ perovskite at high pressure, *Phys. Rev. B*, 62, 14,750–14,756.

Karki, B. B., R. M. Wentzcovitch, S. de Gironcoli, and S. Baroni (2000b), High-pressure lattice dynamics and thermoelasticity of MgO, *Phys. Rev. B*, 61, 8793–8800, doi:10.1103/PhysRevB.61.8793.

Katsura, T., et al. (2004), Thermal expansion of Mg2SiO4 ringwoodite at high pressures, *J. Geophys. Res.*, 109, B12209, doi:10.1029/2004JB003094.

Li, B. (2003), Compressional and shear wave velocities of ringwoodite γ-Mg₂SiO₄ to 12 GPa, *Am. Mineral.*, 88, 1312–1317.

Matsui, M. (1999), Computer simulation of the Mg₂SiO₄ phases with application to the 410 km seismic discontinuity, *Phys. Earth Planet. Inter.*, 116, 9–18.

McMillan, P., and M. Akaogi (1987), Raman spectra of β-Mg₂SiO₄ (modified spinel) and γ-Mg₂SiO₄ (spinel), *Am. Mineral.*, 72, 361–364.

Meng, Y., et al. (1993), In situ high *P-T* X ray diffraction studies on three polymorphs (α, β, γ) of Mg₂SiO₄, *J. Geophys. Res.*, 98, 22,199–22,207.

Meng, Y., Y. Fei, D. J. Weidner, G. D. Gwanmesia, and J. Hu (1994), Hydrostatic compression of γ-Mg₂SiO₄ to mantle pressures and 700 K: Thermal equation of state and related thermoelastic properties, *Phys. Chem. Miner.*, 21, 407–412.

Monkhorst, H. J., and J. D. Pack (1976), Special points for brillouin-zone integrations, *Phys. Rev. B*, 13, 5188–5192.

Perdew, J. P., and A. Zunger (1981), Self-interaction correction to density-functional approximations for many-electron systems, *Phys. Rev. B*, 23, 5048–5079.

Perdew, J. P., K. Burke, and M. Ernzerhof (1996), Generalized gradient approximation made simple, *Phys. Rev. Lett.*, 77, 3865–3868, doi:10.1103/PhysRevLett.77.3865.

Piekarz, P., P. T. Jochym, K. Parlinski, and J. Lazewski (2002), High-pressure and thermal properties of γ-Mg₂SiO₄ from first-principles calculations, *J. Chem. Phys.*, 117, 3340–3344.

Price, G. D., S. C. Parker, and M. Leslieand (1987), The lattice dynamics and thermodynamics of the Mg₂SiO₄ polymorphs, *Phys. Chem. Miner.*, 15, 181–190.

Suzuki, I., E. Ohtani, and M. Kumazawa (1979), Thermal expansion of γ-Mg₂SiO₄, *J. Phys. Earth*, 27, 53–61.

Troullier, N., and J. L. Martins (1991), Efficient pseudopotentials for plane-wave calculations, *Phys. Rev. B*, 43, 1993–2006.

Tsuchiya, T., R. Caracas, and J. Tsuchiya (2004), First principles determination of the phase boundaries of high-pressure polymorphs of silica, *Geophys. Res. Lett.*, 31, L11610, doi:10.1029/2004GL019649.

Tsuchiya, J., T. Tsuchiya, and R. M. Wentzcovitch (2005), Vibrational and thermodynamic properties of MgSiO₃ postperovskite, *J. Geophys. Res.*, 110, B02204, doi:10.1029/2004JB003409.

Watanabe, H. (1982), Thermochemical properties of synthetic high pressure compounds relevant to the Earth's mantle, in *High Pressure Research in Geophysics*, edited by S. Akimoto and M. Manghnani, pp. 441–464, Center for Acad. Publ. of Jpn., Tokyo.

Weidner, D. J., H. Sawamoto, S. Sasaki, and M. Kumazawa (1984), Single-crystal elastic properties of the spinel phase of Mg₂SiO₄, *J. Geophys. Res.*, 89, 7852–7860.

Wentzcovitch, R. M., B. B. Karki, M. Cococcioni, and S. de Gironcoli (2004a), Thermoelastic properties of MgSiO₃-Perovskite: Insights on the Nature of the Earth's Lower Mantle, *Phys. Rev. Lett.*, 92(1), 018501.

Wentzcovitch, R. M., L. Stixrude, B. B. Karki, and B. Kiefer (2004b), Akimotoite to perovskite phase transition in MgSiO₃, *Geophys. Res. Lett.*, 31, L10611, doi:10.1029/2004GL019704.

————————————
R. M. Wentzcovitch and Y. G. Yu, Department of Chemical Engineering and Materials Science, Minnesota Supercomputing Institute for Digital Technology and Advanced Computations, University of Minnesota, 421 Washington Avenue SE, Minneapolis, MN 55455, USA. (wentzcov@cems.umn.edu; yonggang@cems.umn.edu)